



# Modeling Cyclic Capacitive Loading of Thin-Film Batteries

K. Teichert<sup>\*,z</sup> and K. Oldham

Mechanical Engineering, University of Michigan, Ann Arbor, Michigan 48109, USA

Previous modeling of thin-film batteries has primarily looked at simple discharge loads. This work examines modeling of mid-frequency dynamic loads with large variation in current during repetitive loading cycles, a type of loading that is very common in microelectromechanical system (MEMS) applications. Here we show an extension of traditional modeling of thin-film batteries to account for switching and capacitive loading representing piezoelectric or electrostatic microactuation. This model captures behavior at both fast and slow timescales, including effects of short-duration, high-current spikes. We show validation of the model and introduce a cycle projection scheme that allows for over 94% reduction in numerical calculations over a full battery discharge which includes over a million cycles.

© The Author(s) 2017. Published by ECS. This is an open access article distributed under the terms of the Creative Commons Attribution 4.0 License (CC BY, <http://creativecommons.org/licenses/by/4.0/>), which permits unrestricted reuse of the work in any medium, provided the original work is properly cited. [DOI: [10.1149/2.1141702jes](https://doi.org/10.1149/2.1141702jes)] All rights reserved.



Manuscript submitted October 6, 2016; revised manuscript received December 2, 2016. Published January 5, 2017.

Limitations of available power sources, such as batteries, place significant constraints on design of engineered systems at many scales, from vehicles to microelectromechanical systems (MEMS).<sup>1</sup> Battery modeling can be used to help navigate these limitations, and many different modeling approaches have been developed.<sup>2,3</sup> This work focuses on adapting existing modeling approaches to capture cyclic, capacitive loading (i.e. repeated charging of a load that behaves approximately like a capacitor) of thin-film batteries, a loading which is very common in, for example, MEMS applications. Additionally, for small-scale systems, all-solid-state batteries are an attractive alternative to more traditional liquid electrolyte constructs in that sealing of the liquid electrolyte is avoided,<sup>4</sup> generally providing better size and assembly compatibility with micromachined devices. These solid electrolytes typically have lower ionic conductivities, but the effects of this are mitigated by the reduced thickness at which these thin films can be deposited.<sup>5</sup> Various studies have looked at the different properties of various battery chemistries and configurations,<sup>5-12</sup> which is still a very active area of research. However, modeling of cyclic capacitive loads seems to be lacking in the literature.

Understanding the implications of cyclic loading on batteries is important. There have been mixed reports on the broader loading category of intermittent loads on batteries at various scales. Several reports have indicated that loading conditions can have substantial effects on the battery output ability. Fuller et al.<sup>13</sup> discussed different relaxation phenomena in lithium-ion insertion batteries. Feeney et al.<sup>14</sup> recently demonstrated, on a specific primary Li-ion battery, the effect of loading conditions on overall battery capacity utilization, using square wave resistive loads. In that study, experimental results were used to show that the duty cycle had a significant impact on the battery's usable capacity. In an earlier work from Park et al.,<sup>15</sup> experimental results also showed that loading conditions have a significant impact on battery usable capacity. Their work was based on the load created by a DCDC converter. In contrast, Castillo et al.<sup>16</sup> provides experimental observations for intermittent discharge showing no effect for Li-ion rechargeable batteries. It should be noted that the conditions, batteries, and loadings are not consistent in these studies, but rather highlight the potential difficulty of fully understanding and modeling intermittent loading conditions.

In applications such as MEMS, understanding loading effects on the battery will be important in light of small system size, weight, and power targets. MEMS-based micro-robots, for example, must operate under very strict power limits and with finite power system payload capacity. Often, electrical circuitry for low powered application can also be very inefficient,<sup>17</sup> requiring additional battery capacity which can come at a premium in the often "footprint limited" area of MEMS. Moreover, some of the most common MEMS transduction

mechanisms (i.e. electrostatic, piezoelectric) act as primarily capacitive loads resulting in high-speed, high-current intermittent discharge from batteries, which is both less common and less desirable in most larger-scale battery applications. Piezoelectrically-actuated walking micro-robots,<sup>17,18</sup> give a platform for understanding these types of loading conditions having mid-range operating frequencies ( $10^1$ - $10^3$  Hz) and small capacitances ( $10^{-10}$ - $10^{-8}$  F).

As stated above, the purpose of this work is to adapt existing modeling approaches to capture cyclic, capacitive loading of thin-film batteries. There are several challenges with modeling and analyzing this type of loading condition, yet by proper modeling, greater understanding and direction can be had in design and control. Recently we experimentally showed effects of switching capacitive loads on voltage profiles of battery outputs.<sup>19</sup> That work highlighted various phenomena related to the loading and circuitry, and presented a brief demonstration of one cycle of this modeling approach without modeling details. Here we detail the incorporation of key phenomena into a full switching model to capture effects of cyclic capacitive loading on thin-film batteries. We choose to use an electrochemical approach to more readily correlate between physical properties and the model parameters. This model was based heavily on work presented by Fabre et al.<sup>2</sup> and Danilov et al.<sup>20</sup> and more detailed descriptions of the electrochemical equations can be found there, as well as prior work by Thomas et al.<sup>21</sup> This basic model foundation was then adapted for our loading conditions as well as to include switching and other phenomena seen experimentally.<sup>19</sup> Model parameters were found using a fitting optimization approach that was developed to correlate the model with experimental data.

Meanwhile, to model faster timescale dynamics of cycling requires a significant numerical cost. A typical battery discharge in our testing could be over a million cycles for some of the tests run. In order to show model responses across the full battery discharge, a projection approach was developed that allowed for projecting battery states over many cycles to reduce numerical modeling costs. By incorporating system characteristics of cyclic capacitive loads on thin-film batteries at very different timescales and current levels, this combined modeling and simulation approach should enable greater understanding and capabilities in design and control of devices operating in this manner.

## Modeling Development

**Modeling background and assumptions.**—Two widely used approaches for battery modeling are equivalent circuit modeling, where battery responses are modeled using an analogous electrical circuit,<sup>3,22-24</sup> and physics-based models.<sup>2,20,25</sup> This work is based on physics-based approaches, adapted from solid-state battery modeling presented by Fabre et al.<sup>2</sup> and Danilov et al.<sup>20</sup> We expand the use of this model to account for and investigate fast dynamics in the electrochemical system. Fabre's model gives a 1-dimensional description of an all solid-state thin-film Li/LiPON/Li<sub>y</sub>CoO<sub>2</sub> battery with the

\*Electrochemical Society Student Member.

<sup>z</sup>E-mail: [kbt@umich.edu](mailto:kbt@umich.edu)

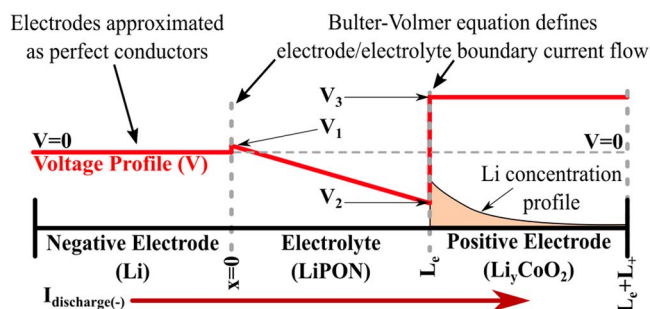


**Figure 1.** Battery schematic. A typical voltage profile for the model is shown on the coordinate system. A theoretical concentration profile for the positive electrode is shown also.

following assumptions made to simplify the problem: (1) isothermal behavior with no self-heating, (2) Li electrode acts as a perfect conductor with negligible voltage drop, (3) negligible volume changes, and (4) constant electrolyte concentration/conductivity. In this work we choose to neglect the voltage drop in the positive electrode. At conditions where constant electrolyte conductivity can be approximated it is assumed that the resistive drop in the positive electrode will be moderate (e.g. using the conductivity of  $\text{LiCoO}_2$  in Park et al.,<sup>26</sup> and the parameters approximated later in this work the positive electrode resistance would be  $\sim 3\%$  of that of the electrolyte) and can be compensated for in other parameters. Under this assumption and in light of the increased simplicity of modeling (reduction of unknowns from 5 to 4), this approximation seemed justified. In this paper the loading applied (10 nF 100 Hz) allows the battery significant time to recover between major switch/charging events, at higher frequencies or higher average currents both the electrolyte conductivity and the positive electrode resistance assumptions (in addition to other limiting assumptions) will likely need to be readdressed. Finally, only battery discharge is considered.

Key equations for the model will be given here; for a more thorough derivation see the source literature.<sup>2,20,21</sup> Notation will be kept similar to the source literature for convenience. The coordinate system and battery schematic are shown in Fig. 1 and remain similar to Fabre et al.,<sup>2</sup> where the boundary of the negative electrode/electrolyte is set as zero ( $x = 0$ ). Voltages are defined as:  $V_0 = 0$ , the voltage of the negative electrode which is set as a reference;  $V_1$ , the voltage on the electrolyte side of the negative electrode/electrolyte interface;  $V_2$ , the voltage on the electrolyte side of the positive electrode/electrolyte interface; and  $V_3$ , the voltage of the positive electrode.

**Electrochemical model equations.**—The model is based on current balance through the battery. Current flows through the electrode/electrolyte interfaces are expressed using the Butler-Volmer equation and are defined as follows: across the negative electrode/electrolyte interface ( $x = 0$ )

$$\frac{I}{A} = i_{0,-} \left( \exp\left(\frac{\alpha_{a,-} F (V_0 - V_1)}{RT}\right) - \exp\left(-\frac{\alpha_{c,-} F (V_0 - V_1)}{RT}\right) \right); \quad [1]$$

and across the electrolyte/positive electrode interface ( $x = L_e$ )

$$\frac{I}{A} = i_{0,+} \left( \exp\left(\frac{\alpha_{a,+} F (V_3 - V_2 - U)}{RT}\right) - \exp\left(-\frac{\alpha_{c,+} F (V_3 - V_2 - U)}{RT}\right) \right), \quad [2]$$

where  $I$  is the current,  $A$  is the cross sectional area,  $i_0$  is the exchange current density with subscripts (+,-) indicating positive and negative electrodes respectively,  $\alpha$  is the charge transfer coefficient with subscripts ( $a,c$ ) denoting anodic and cathodic reactions at the given interface,  $F$  is Faraday's constant,  $R$  is the gas constant,  $T$  is temperature

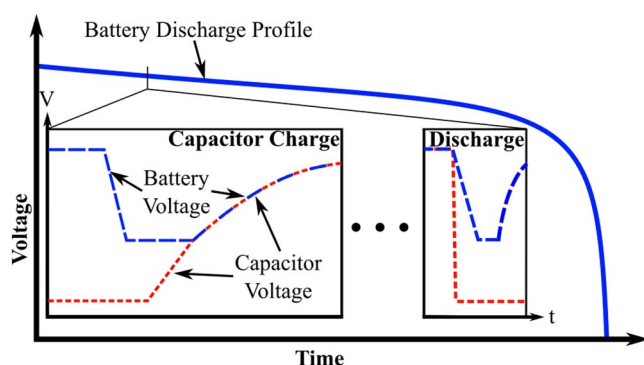


**Figure 2.** Battery discharge schematic. Switching dynamics have various timescales in these applications. The various switching times are represented in the subfigure.

in Kelvin, and  $U$  is the open circuit potential (derived from a combination of experimental data and datasheet information<sup>27</sup>). Diffusion in the  $\text{Li}_y\text{CoO}_2$  positive electrode is described as:

$$\frac{\partial c_+}{\partial t} = \frac{\partial}{\partial x} \left( D_+ \left( \frac{c_+}{c_{+,max}} \right) \frac{\partial c_+}{\partial x} \right) \text{ at } L_e < x < L_e + L_+ \quad [3]$$

$$D_+ \left( \frac{c_+}{c_{+,max}} \right) = D_{+,0} \times D_{+,norm} \left( \frac{c_+}{c_{+,max}} \right) \quad [4]$$

with  $c_+(x)$  the concentration in the positive electrode as a function of  $x$ , the subscript max denoting the maximum concentration,  $D_{+,0}$  the nominal diffusion coefficient,  $D_{+,norm} \left( \frac{c_+}{c_{+,max}} \right)$  a concentration dependent function of the normalized diffusion coefficient, and  $L_e$  and  $L_+$  the thicknesses of the electrolyte and positive electrode respectively. Boundary conditions are given as:

$$\frac{\partial c_+}{\partial x} = 0 \text{ at } x = L_e + L_+ \quad [5]$$

$$\frac{\partial c_+}{\partial x} = \frac{I}{AFD_+} \text{ at } x = L_e \quad [6]$$

In Fabre et al.<sup>2</sup> the electrolyte concentration and conductivity are approximated as constant which is adequate for low current applications. We do the same, though for higher average current applications this would likely need to be revisited. The electrolyte resistance is defined as:

$$R_e = \frac{V_2 - V_1}{I} \approx \frac{V_{Batt,Nom} L_e}{FD_{e,0} c_e A} \quad [7]$$

With  $D_{0,e}$  the electrolyte diffusion coefficient,  $c_e$  the electrolyte Li concentration, and  $V_{Batt,Nom}$  is the nominal battery voltage (taken as 4.1 V in this work). Equations 1–3 and 7, define the system of four equations and four unknowns (i.e.  $V_1$ ,  $V_2$ ,  $V_3$ , and  $c_+$ ).

**Cyclic capacitive load modeling.**—Next, modeling is extended to account for effects of cyclic capacitive loading on thin film batteries, primarily through additional load dynamics. Previous solid-state battery analysis has focused primarily on other loading conditions such as constant current or voltage, with limited information on capacitive loads,<sup>28</sup> so to better understand what additional phenomena are important to incorporate into a model with capacitive loading, initial experimental work was performed. A conceptual representation of this is shown in Figure 2. Experimentally, a simple H-bridge switching circuit was used to cycle a 50 $\mu\text{Ah}$  battery over various capacitive loads. The basic circuit schematic is shown in Figure 3. Details of experimental setup and findings were reported elsewhere demonstrating the importance of consideration of these losses.<sup>19</sup> Key findings are summarized here.

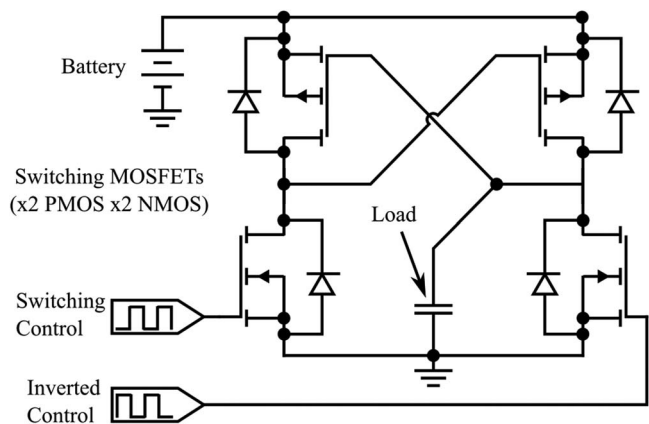


**Figure 3.** H-bridge switching circuitry for experimental testing. Reprinted with permission,<sup>19</sup> and based on the circuit presented by others.<sup>29</sup>

Timescale considerations: It is noted that timescales of the capacitor charging, battery dynamics, and switching characteristics can be very similar and therefore may all need to be addressed during individual cycle modeling (e.g. the battery cannot be assumed to be a perfect power source, and switching cannot be assumed to be instantaneous). Conversely, changes in system aspects such as open circuit potential and diffusion coefficient can occur over time scales that are orders-of-magnitude longer (minutes or hours vs. microseconds), which makes simulation over the full battery discharge challenging.

Switching and leakage losses: The switching circuit used to drive the capacitive load was not optimized and suffered from substantial losses; however, investigation of those losses was instructive, and necessary for comparison of modeling and experimental data. These losses included a short period where a limited path to ground was made during switching, while switching transistors were only partially charged. Additionally, it appeared that there continued to be transient switching losses at least until the switching was nearly completed. As in any transistor-based circuit, there was also a voltage dependent leakage current in the system. Frequency and size of capacitive loading influenced which type of loss was dominant.

Switching dynamics and timing: The timing of the switching phenomena was examined to provide an accurate load to the battery model. Switching characteristics and approximate equivalent loading for capacitor charging (switch on) and discharging (switch off) are given in Figures 4 and 5. Again for more information on experimental setup and results see our prior work.<sup>19</sup> The main switching events, common in many switching circuits, included the following (shown graphically in Figure 2):

1. Switching Initiated ( $t_{switch} \leq t \leq t_{hold}$ ): This is characterized by a sharp drop in battery voltage as the H-bridge transistors are between equilibrium states creating a limited path to ground through the switching circuitry. Battery voltage drops to the threshold voltage dictated by the switching components ( $V_{th}$ ). This timing was determined separately for on and off switching. For general applications, momentary connection to ground can be reduced or eliminated with more complex circuit design, though often with a tradeoff of greater complexity, larger leakage current, and/or slower response times. Switching circuit optimization was not the purpose of this work. For capacitor discharge, the load capacitor is considered disconnected from the battery and the voltage is removed.
2. Switching Delay ( $t_{hold} \leq t \leq t_{charge}$ ): There is then a short period of time before the capacitor begins to charge (switch on/capacitor charge) or the battery begins to recover (switch off/capacitor discharge) where there remains a limited path to ground through the switch. During initial switching, a large current spike is observed leaving the battery system. This timing was determined separately for on and off switching.

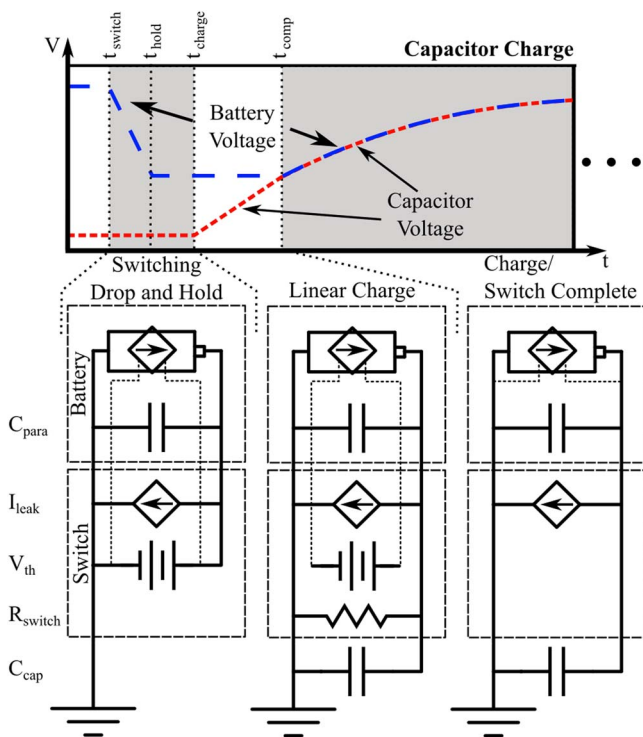


**Figure 4.** Switch timing characteristics and approximate equivalent loading for capacitor charging. The battery is represented as a voltage controlled current source with dotted lines representing the voltage signal.

3. Capacitor Linear Charging ( $t_{charge} \leq t \leq t_{comp}$ ): For switch on (capacitor charge) only, as the capacitor charges the battery is initially voltage limited by the switching transistors which causes a constant, or near constant, current into the capacitor. This current gives a nearly linear increase in the capacitor voltage that increases until the capacitor reaches the threshold.

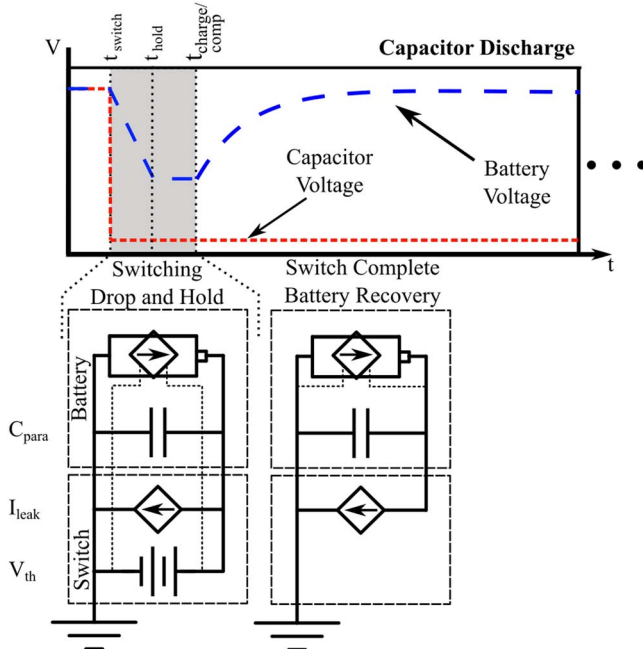


**Figure 5.** Switch timing characteristics and approximate equivalent loading for capacitor discharging. The battery is represented as a voltage controlled current source with dotted lines representing the voltage signal.

4. Switching Complete ( $t_{comp} \leq t$ ): For switch on (capacitor charge), after the capacitor has reached the switching threshold voltage for the H-bridge transistors, the switching is considered completed and the battery and capacitor voltage increase in a somewhat exponential fashion, approximately as would an ideal voltage-resistor-capacitor system. For switch off (capacitor discharge), the battery does not need to supply current to the capacitor so after the switching delay the battery begins to recover immediately and the switching is considered completed.

Parasitic capacitance: Parasitic capacitance was manifested in several ways in the battery system. It was not determined if this was from the battery, or some other source (e.g. packaging or electrodes). This capacitance allowed for a small portion of the battery's charge to be stored in a quickly accessible format that was discharged to ground during the switching. This capacitance is in the range of the loads applied and has a substantial effect on charging dynamics.

During the capacitor charging mode of the cycle (switch on, battery discharging), loading on the battery includes switching effects, linear/exponential charging of the capacitor, and parasitic capacitor charging. Capacitive loading was applied to the model by dictating the battery voltage (i.e. capacitor voltage or threshold voltage) for short time steps, and calculating the battery response. At each time step in the model, the current available from the battery was determined based on the battery voltage,  $V_{Batt}$ , imposed by the load and the lithium concentration at the positive electrode/electrolyte interface. This current is a combination of current lost through leakage ( $I_{leak}$ ) and switching ( $I_{switch}$ ), as well as current into the load ( $I_{cap}$ ) and parasitic capacitors ( $I_{para}$ ),

$$I(t) = f\left(\frac{c_+}{c_{+,max}}, V_{Batt}(t)\right) = I_{leak} + I_{switch} + I_{cap} + I_{para}. \quad [8]$$

Losses related specifically to the switching events (primarily  $I_{switch}$ ) were seen in two separate timeframes of the switching, and different modeling approaches were used for each of the two. The first part is for time  $t_{switch} \leq t \leq t_{hold}$  during which the battery has a limited path to ground through the switch. The current out of the battery during this time at the given voltages is all lost to ground. During this time the parasitic capacitor tracks the battery voltage from the battery voltage at the time of switching,  $V_{Batt}(t_{switch})$ , to the switching threshold voltage,  $V_{th}$ , and that charge is considered lost to ground as well. The second switching loss period is  $t_{hold} \leq t \leq t_{comp}$  (only applies to switch on/capacitor charge) where the battery is now charging the capacitor. These losses were approximated as a set resistance to ground,  $R_{switch}$ , in parallel with the load capacitor.

During capacitor discharge mode of the cycle (switch off, battery disconnected), we again see the switching effects, but only parasitic capacitor charging occurs as the battery recovers from the switch. All loading in the model can be described as an imposed voltage load on the battery. The battery voltage ( $V_{Batt}$ ) corresponds to  $V_3$  in Eq. 2 and is equal to the voltage on the parasitic capacitor ( $V_{para}$ ). As the battery recovers, its voltage is dictated by the charge on the parasitic and load capacitors. This dependence gives interplay between voltage and current. Loading is shown in Eqs. 9 and 10.

$$\frac{V_{Batt}}{V_{para}} = \begin{cases} \text{For Switch ON and OFF} \\ V_{Batt}(t_{switch}) - \frac{t-t_{switch}}{t_{hold}-t_{switch}}(V_{Batt}(t_{switch}) - V_{th}), t_{switch} \leq t \leq t_{hold} \\ V_{th}, t_{hold} < t \leq t_{comp} \\ \text{For Switch ON only} \\ V_{th} + \Delta V_{cap}, t_{comp} < t \\ \text{For Switch OFF only} \\ V_{th} + \Delta V_{para}, t_{comp} < t \end{cases} \quad [9]$$

$$V_{cap} = \begin{cases} \text{For Switch ON Only} \\ 0, t_{switch} \leq t \leq t_{charge} \\ \Delta V_{cap,linear}, t_{charge} < t < t_{comp} \\ \Delta V_{cap}, t_{comp} \leq t \\ \text{For Switch OFF Only} \\ 0, t_{switch} \leq t \end{cases} \quad [10]$$

Here  $C_{cap}$  and  $C_{para}$  are the capacitances of the load and parasitic capacitors. The subscript "linear" refers to the portion of time when the capacitor charges at a near constant rate. The dynamics of the capacitor voltage after it is switched off are not tracked, and approximated as no longer connected to the battery.

**Nondimensional model parameters.**—This system has vastly different timescales and length scales. The timescales will be discussed later, but in both length and timescales there are several orders of magnitude variations (e.g. thickness of the electrode may be a few microns but surface area is on the order of a  $\text{cm}^2$ ). In order to deal with some of these disparities the model was nondimensionalized (an example of electrochemical normalization can be found in Deshpande et al<sup>30</sup>). This also allows us to consolidate parameters resulting in the final nondimensional parameters,  $\pi$ , and coefficients for non-dimensionalizing time and capacity,  $\varphi_1$  and  $\varphi_2$ , as follows:

$$\varphi_1 = \frac{D_{+,0}}{L_+^2} \left[ \frac{1}{s} \right] \quad [11]$$

$$\varphi_2 = \frac{2}{A \times F \times c_{+,max} \times L_+} \left[ \frac{1}{As} \right] \quad [12]$$

$$\pi_1 = \alpha_{a,+} \quad [13]$$

$$\pi_2 = \frac{c_e}{c_{e,max}} \quad [14]$$

$$\pi_3 = \frac{D_{+,0} \times c_{+,max} \times L_e}{D_{e,0} \times c_{e,max} \times L_+} \quad [15]$$

$$\pi_4 = \left( \frac{2i_{0+,max} \times L_+}{F \times c_{+,max} \times D_{+,0}} \right) \left( \frac{c_e}{c_{e,max}} \right)^{-\alpha_{a,+}} \quad [16]$$

$$\pi_5 = \left( \frac{2i_{0-,max} \times L_+}{F \times c_{+,max} \times D_{+,0}} \right) \left( 1 - \frac{c_e}{c_{e,max}} \right)^{\alpha_{a,-}-1} \left( \frac{c_e}{c_{e,max}} \right)^{-\alpha_{a,-}} \quad [17]$$

$$\pi_6 = \frac{2C_{para} \times V_{Batt,Nom}}{F \times c_{+,max} \times A \times L_+} \quad [18]$$

$$\pi_7 = \frac{2V_{Batt,Nom} \times L_+}{R_{switch} \times F \times c_{+,max} \times A \times D_{+,0}} \quad [19]$$

Eq. 11 represents time normalization. Eq. 12 represents the current normalization in the positive electrode. Equations 13–17 are parameters of the model connected with the electrolyte and/or the electrolyte/electrode interactions with  $D_{e,0}$  the diffusion coefficient of the electrolyte and the subscript *max* for the exchange current density indicating the maximum value. Eqs. 18 and 19 are parameters regarding the parasitic capacitance and the losses in the switching respectively with  $V_{Batt,Nom}$  the nominal charged battery voltage (for this work 4.1V).

**Numerical implementation.**—Numerical implementation was done similar to Fabre et al.,<sup>2</sup> using the Crank-Nicholson approach applied to the Lithium concentration profile in the LiCoO<sub>2</sub> (positive electrode) and optimization to balance currents. Initial Crank-Nicholson coding was based on methods presented by Spender and Ware,<sup>31</sup> and adapted heavily for the current work. Care needed to be taken for the Neumann boundary conditions in our model. In particular, the large spikes in current cause significant changes in the concentration at the boundary between the positive electrode and the electrolyte. Because of these sharp gradients a very fine discretization was needed near the boundary; however, further in the positive electrode a much coarser grid was adequate. To accommodate the boundary and yet save on computational expense a non-uniform mesh was used. This was implemented based on the equations in the appendix of Bowen and Smith.<sup>32</sup> Time discretization was also varied to capture the areas of faster dynamics with greater accuracy.

**Parameter fitting.**—Parameter fitting was implemented to correlate the non-dimensional parameters with corresponding experimental data. Fitting was performed using a combination of two types of data: a suite of constant current tests and a single charge/discharge cycle of a capacitor (with validation over a full battery discharge). Using these two data sets it was anticipated that we could fit the fast and slow dynamics of the battery model. The switching fit was performed primarily around the area of large dynamic changes. Errors in fitting were determined from differences in the voltages, timing, and capacity loss (single cycle), of model and experimental data.

Weighting of different aspects of the calibration process was chosen. A variety of different optimization steps were used to target specific parameters. Weighting was chosen to primary priority on switch timing and the voltage before each switch. This voltage is key in that it describes the charge transferred to the capacitor, which is one of the most accurately known variables experimentally. The shape of the capacitor charge was generally given lower priority in the weighting. This was done in part because of the higher-order dynamics that seemed to be at play beyond the fitting capabilities of the model that limit the possible fit. It is not anticipated that a significantly better fit of the capacitor charging profile could be obtained with changing weighting. Low weighting was also given to the highest current of the constant current set because model assumptions break down at high currents, while higher weighting was often given to the lowest current run.

Multiple iterations of a direct search method with an adaptive mesh (patternsearch function in MATLAB) were used to perform the optimization. In addition to these parameter fits, certain characteristics of the variable diffusion coefficient were also fit to allow the model to mimic in part the concentration dependency of the diffusion coefficient that is described in Fabre et al.<sup>2</sup> Switching parameter times were determined from averaging experimental data.

**Full battery discharge modeling.**—Modeling effects of many cycles of the load is important in understanding full battery responses and implications of the loading for desired applications. However, analyzing the load effects over time can be challenging due to the differences in timescale. In order to demonstrate our model's use at various stages of the battery discharge we implemented a transition matrix projection approach. There may be other approaches that could also be used, such as the method of multiple scales.

The projection approach developed was as follows. Let the dimensionless Lithium concentration in the positive electrode be discretized in time and space as:

$$\frac{c_+(x, t)}{c_{+,max}} = y(x, t) \rightarrow y(m, n) \equiv y_n^m \quad [20]$$

where,  $k$ , is the spatial grid point, and  $n$  is the cycle number. The full profile vector after a given cycle noted as  $\bar{y}_n$ . It is then possible to describe the battery in terms of the concentration profile changes

from cycle to cycle.

$$\bar{y}_{n+1} = f(\bar{y}_n) \quad [21]$$

where  $f$  is a function representing the battery dynamics for a given set of parameters such as capacitor load size, cycle frequency, etc. If  $f$  is approximated as a linear function near the current operating point then delta change in concentration per cycle,  $\Delta\bar{y}_{n+1}$ , can be written as:

$$\Delta\bar{y}_{n+1} \equiv \bar{y}_{n+1} - \bar{y}_n = f(\bar{y}_n) - f(\bar{y}_{n-1}) = g(\Delta\bar{y}_n) \approx T\Delta\bar{y}_n \quad [22]$$

The matrix  $T$  is a linearized transition matrix for the delta change in concentration profile of the positive electrode during cycle  $n$  to the delta change in concentration during cycle  $n+1$ . That is, we take the delta change in concentration profile,  $\Delta\bar{y}_n$ , as the states of the system for a given cycle. We determined  $T$  using a perturbation method on  $\Delta\bar{y}_n$ . By perturbing each grid point by some  $\delta^m$ , we can determine the change to every other grid point,  $\epsilon_m^i$ , where  $m$  denotes the grid point being perturbed, and  $i$  indicates the affected grid point:

$$g\left(\begin{bmatrix} \Delta y_n^1 \\ \Delta y_n^2 \\ \vdots \\ \Delta y_n^m + \delta^m \\ \vdots \\ \Delta y_n^k \end{bmatrix}\right) = \begin{bmatrix} \Delta y_{n+1}^1 + \epsilon_m^1 \\ \Delta y_{n+1}^2 + \epsilon_m^2 \\ \vdots \\ \Delta y_{n+1}^m + \epsilon_m^m \\ \vdots \\ \Delta y_{n+1}^k + \epsilon_m^k \end{bmatrix} \quad [23]$$

Assuming a constant  $\delta^m = \delta$ , we can construct the transition matrix:

$$T = \begin{bmatrix} T_1^1 & T_2^1 & \dots & T_k^1 \\ T_1^2 & T_2^2 & \dots & T_k^2 \\ \vdots & \vdots & \ddots & \vdots \\ T_1^k & T_2^k & \dots & T_k^k \end{bmatrix} = \delta \begin{bmatrix} \epsilon_1^1 & \epsilon_2^1 & \dots & \epsilon_k^1 \\ \epsilon_1^2 & \epsilon_2^2 & \dots & \epsilon_k^2 \\ \vdots & \vdots & \ddots & \vdots \\ \epsilon_1^k & \epsilon_2^k & \dots & \epsilon_k^k \end{bmatrix} \quad [24]$$

One further numerical challenge of the electrochemical system noted earlier is that it is naturally sequential where the solution for the first step must be solved in order to determine the next step. Because of this, we can take little advantage of parallel computing. Determining the transition matrix in the manner presented here allows some of the computation (the perturbed cycles) to be performed in parallel with ongoing simulation cycles, reducing the sequential numerical burden.

The transition matrix,  $T$ , allows us to now project forward the system states,  $\Delta\bar{y}_n$ ,  $p$  cycles into the future, which can be used to determine the concentration profile as:

$$\bar{y}_{n+p} = \bar{y}_n + \sum_{j=1}^p T^{j-1} \Delta\bar{y}_n. \quad [25]$$

It is important to remember that this assumes a linear system. However, this problem has a number of nonlinear aspects (e.g. the OCV, electrochemical equations, and variable diffusion coefficient). These nonlinearities introduce error that generally increases with projection length (i.e., the number of cycles projected using a fixed transition matrix approximation). An approach used in this work to reduce this error was to update the transition matrix before each projection. A flowchart of the model and projection process are given in Figure 6.

## Results

**Experimental data.**—Three sets of experimental data were used, two for calibration and parameter fitting, and the other for model validation. The first set of calibration data consisted of five different constant current tests including 5  $\mu\text{A}$  (0.1 C), 20  $\mu\text{A}$  (0.4 C), 50  $\mu\text{A}$  (1 C), 200  $\mu\text{A}$  (4 C), and 500  $\mu\text{A}$  (10 C). This constant current data was gathered using a Labview setup with the current regulated by a Keithley sourcemeter. Losses and other effects were not considered when collecting this data.

Switching data was also acquired where a 10 nF capacitor was cycled at 100 Hz. Experimental setup and limitations are reported

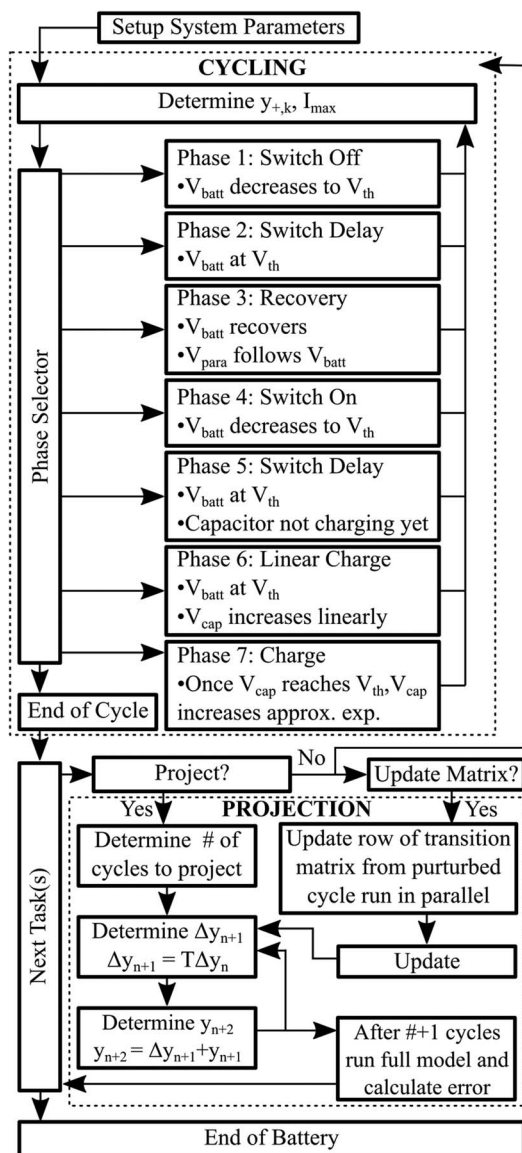


Figure 6. Flowchart of cyclic model and projection approach.

elsewhere.<sup>19</sup> The main limitations in the data included accuracy in the current data and conversion from AC probe readings to DC values, as well as noise and other extraneous effects in the current and voltage measurements. Two sets of switching tests were used. The first was used for calibration, and only measurements from a single cycle near the beginning of battery discharge were used. The second was used for validation of the model, using the full battery discharge data.

When converting these datasets to overall battery capacities, the constant current data was significantly different from the values published in the vendor literature compared to that of the switching data. This could be in part due to the differences in setup, or assumptions, or variations between tests due to battery/run variations. To correlate the data for model validation purposes, the constant current data was scaled using an interpolated capacity of the average current for the switching data (15  $\mu\text{A}$ ). Therefore the data presented here is used primarily for model approach validation, and is not necessarily representative of general capabilities of the specific battery type that was used.

All experimental runs charged the battery to  $\sim 4.1$  V and discharged until  $\sim 3.3$  V. These voltages in the open circuit potential

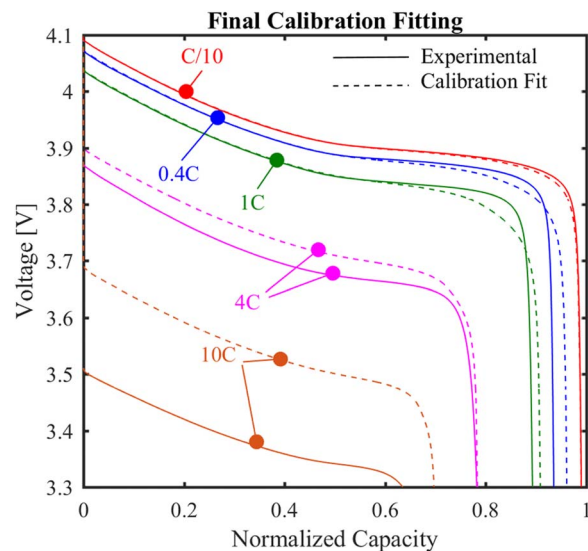


Figure 7. Constant current profiles and calibrated fits.

were approximated as being 0.5 and 1.0 values of the normalized lithium concentration in the positive electrode.

**Parameter fitting/calibration.**—Parameter fitting was used to extract  $\phi_1$ - $\phi_2$  and  $\pi_1$ - $\pi_7$  in Equations 11–19 and select points defining the concentration dependent diffusion coefficient. As noted one cycle of a 10 nF capacitor at 100 Hz was used in connection with the constant current data. The area of the battery was approximated based on the die size. Switch drop and hold times as well as threshold voltage were averaged from experimental data (but could be taken from a single data set), and are constant throughout the full model.

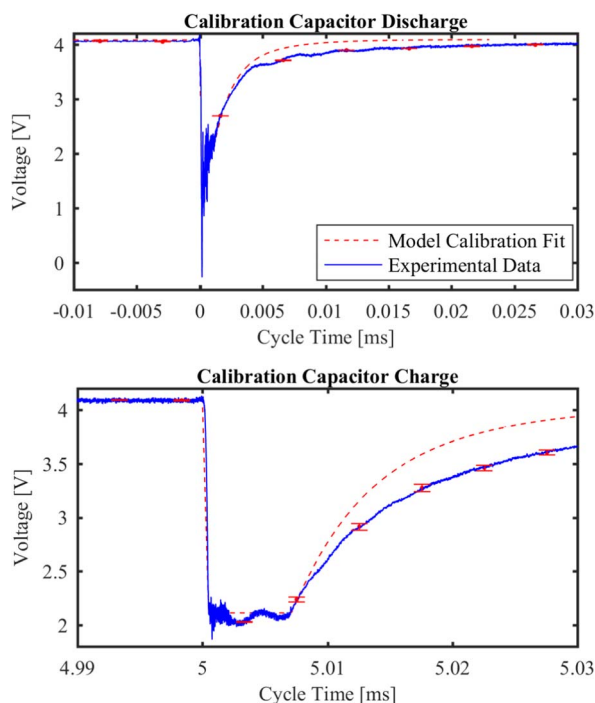


Figure 8. Switching profile data and calibrated fit. Error bars are based on rolling average and discrepancies between battery and capacitor voltage measurements.

**Table I. Calibration parameters. References are for one or more of the parameters in the equation.**

Optimized Parameter	Initial Value	Final Value	Ref Value Included in Parameter	Corresponds to:
$\varphi_1 [\frac{1}{s}]$	4.54e-2	5.24e-2	$D_{0,+} = 0.2 [\frac{\mu m^2}{s}]^2$	Time
$\varphi_2 [\frac{1}{mA s}]$	5.78e-3	4.17e-3	$c_{+,max} = 5 \times 10^{-14} [\frac{mol}{\mu m^3}]^2$	Positive electrode current and capacity
$\pi_1 [-]$	0.500	0.525	$c_e = 10.818 \times 10^{-15} [\frac{mol}{\mu m^3}] c_{e,max} = 6 \times 10^{-14} [\frac{mol}{\mu m^3}]^{*,20}$	Electrolyte or electrode/electrolyte boundary
$\pi_2 [-]$	0.180	0.191		
$\pi_3 [-]$	0.285	0.285	$D_e = 6 \times 10^{-3} [\frac{\mu m^2}{s}]$ Based on <sup>*,20</sup>	
$\pi_4 [-]$	9.03e-2	1.68e-2	$i_{0+,max} = 4.4 \times 10^{-9} [\frac{mA}{\mu m^2}]^2$	
$\pi_5 [-]$	0.167	0.281	$i_{0-,max} = 1.5 \times 10^{-8} [\frac{mA}{\mu m^2}]^2$	
$\pi_6 [-]$	5.98e-8	6.03e-8		Parasitic capacitance
$\pi_7 [-]$	6.09e-2	7.10e-2		Switching loss
Averaged Parameter	Value	Description		
$V_{th}$	2.112 [V]	Switching threshold voltage		
$t_{drop,on}$	0.124 [ $\mu s$ ]	Battery voltage drop time, switch on ( $t_{switch} - t_{hold}$ )		
$t_{delay,on}$	1.004 [ $\mu s$ ]	Switch delay time, switch on ( $t_{hold} - t_{charge}$ )		
$t_{drop,off}$	0.521 [ $\mu s$ ]	Battery voltage drop time, switch off ( $t_{switch} - t_{hold}$ )		
$t_{delay,off}$	0.069 [ $\mu s$ ]	Switch delay time, switch on ( $t_{hold} - t_{comp}$ )		
Additional Parameter				
$V_{Batt,Nom}$	4.1 [V]	Nominal charged battery voltage		

\*Electrolyte parameters initial values were based on LiPO information.<sup>20</sup>

Thicknesses used in Initial values were approximated as 2.5  $\mu m$  for the positive electrode and 10  $\mu m$  for the electrolyte.

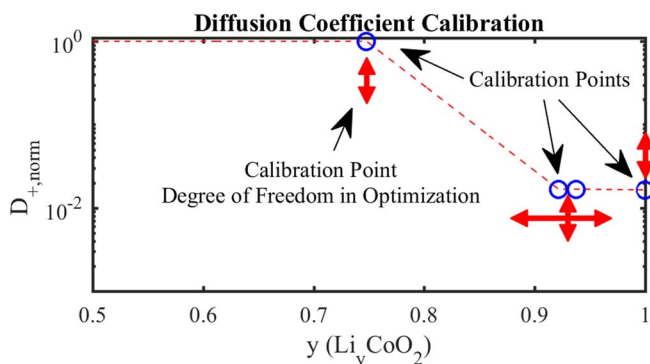


**Figure 9.** Normalized diffusion coefficient calibration. The blue circles in the profile represent points that were allowed to vary within certain limits. The red arrows show the degrees of freedom. The center two points always had the same diffusion coefficient value.

The final parameter fitting results are given in Figures 7–9 and Table I. Figure 9 shows the points defining the diffusion coefficient and the degrees of freedom associated in the optimization. Table II shows physical parameter values based on the nondimensionalized

**Table II. Calculated parameters. Physical parameters were calculated from the calibration parameters based on two assumed values as noted.**

Assumed Parameter	Value
$c_{+,max}$	$5 \times 10^{-14} [\frac{mol}{\mu m^3}]$
$\alpha_{a,-}$	0.5
Calculated Parameter	Value
$D_{0,+}$	$0.428 [\frac{\mu m^2}{s}]$
$L_+$	2.86 [ $\mu m$ ]
$i_{0+,max}$	$2.5 \times 10^{-9} [\frac{mA}{\mu m^2}]$
$i_{0-,max}$	$2.1 \times 10^{-8} [\frac{mA}{\mu m^2}]$
$R_e$	243 [ $\Omega$ ]
$C_{para}$	3.53 [mC]
$R_{switch}$	4.60 [k $\Omega$ ]

parameters and two assumed parameter values. The fitting of the constant current discharge is very close, with the exception of the highest current profile which had low priority in the calibration process. This lack of fit is expected in part due to the assumption of constant electrolyte conductivity, which assumption may need to be addressed if loadings are used that create currents consistently higher than seen in the switching tests presented here.

In the switching fits, it appears that there are higher order dynamics that slow down the charging of the capacitor that are not fully captured by the model. This potentially could be from the switching circuitry as there could still be residual losses from incomplete switching past the time that the battery and capacitor voltages meet. In spite of this, the fast dynamics of the switching are able to be reasonably captured with the model and parameters implemented through the majority of the battery discharge as will be discussed later with validation. Some of the starting parameters for the calibration optimization are based off of LiPO instead of LiPON. It is understood that these will have different properties, but for a starting point for the fitting optimization it was considered adequate. This fitting approach allows for parameter determination using very little high-sample-rate data by being able to base the fit on only one on/off cycle of the capacitor. The majority of the fitting data comes from the coarsely sampled constant current profile that is much easier to attain.

It should be noted that the fitting of the parameters proved to be heavily influenced by the starting point and optimization approach. Precision experimental data and/or an improved calibration approach would be beneficial for more targeted future parameter fitting.

**Validation modeling results.**—Using the parameters determined in calibration, a full battery discharge was modeled, with a cyclic discharge at 100 Hz over a 10 nF capacitor. This validation data set was a separate test run from that used for model fitting and a portion of the capacitor charge of each measured cycle is shown in Figure 10. The discharge profiles are presented to show the changes in cycle profile over the full battery discharge. The experimental data is adjusted so that the switching of the model and each cycle align. Aspects of the switching were incorporated into the model as described. The inputs to the model include the calibration data (parameters, switching times, and threshold voltage), as well as the initial voltage of the validation data set. This is the voltage of the battery, including any effects of leakage current. Because of leakage current in the

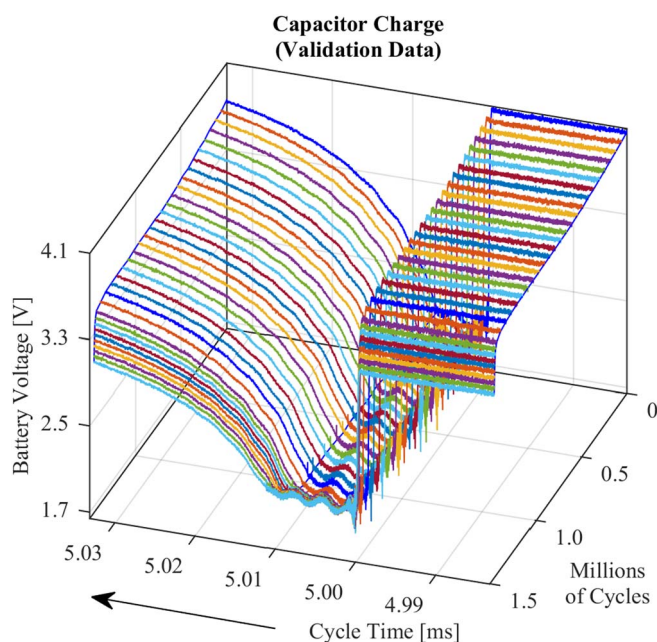


**Figure 10.** Capacitor charge section of the validation data. The battery voltage profile for each measured cycle is shown. Each cycle is aligned to correlate switching times for the model and each cycle. Only capacitor charge data is shown and voltage error bars are omitted.

measurement, the initial concentration is not exactly known but rather is estimated from the voltage with the applied leakage current. The capacitor charge portions of the model and validation data are shown in Figure 11. The key points of the model fit are the voltage before switching, time before the battery begins to recover, and the overall shape of the recovery as the capacitor charges as seen in Figure 12.

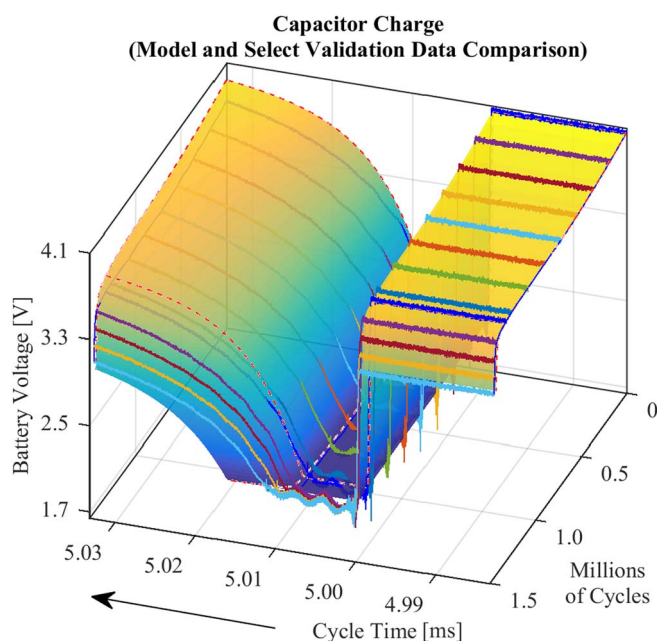


**Figure 11.** Model/select validation data comparison. The model shows a slightly faster charge of the capacitor than the experimental data, however, the final voltages are very similar. The overall battery life also shows good correlation in this scenario. Voltage error bars are omitted on experimental data.

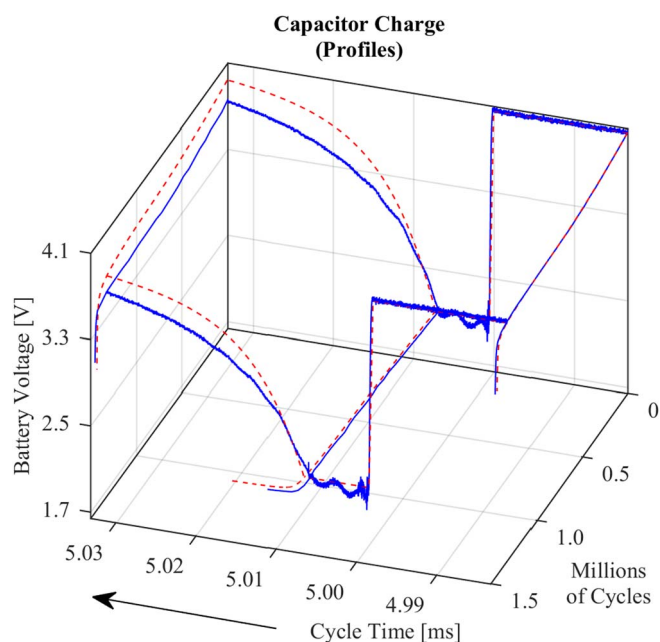


**Figure 12.** The profiles of the model/select validation data comparison are shown. The fit shows that fast and slow dynamics of the battery are represented by the model. Voltage error bars are omitted.

A comparison of the model and validation data current profiles was also performed. However, due to limitations in the experimental current data measurement,<sup>19</sup> comparison of the model current profile and validation data current are used only for reference and are shown in Figure 13. The figure shows the losses in switching and the charge transfer to the capacitor, and indicates some of the limitations of the model. It is important to note that in Figure 13 the leakage current is small enough to not be discernable in the plot, and parasitic capacitor current is based for plotting purposes on the change in battery voltage.

In the full battery discharge model, 300 initial cycles were run before the first projection. Additionally, a certain number of cycles were allowed after each projection to allow the model to settle before beginning updating the transition matrix. The number of cycles to project was determined on a tradeoff between projection size and error. A few additional cycles were used before each projection to determine an appropriate projection/error. The full battery discharge model data shows reasonable agreement with the experimental data. Figure 14 shows a comparison between the experimental and modeled discharge based on the number of cycles performed. Concentration profiles for the full discharge of the battery are shown in Figure 15. The small changes in slope of the concentration at the early cycles may indicate that the diffusion did not play a large role. This is assumed in part to be why large projections during this portion were possible.

A significant computational decrease was able to be achieved using this projection approximation. One measure of this reduction is the ratio of cycles fully modeled to the total number of cycles (including projected cycles). The modeled cycles do not include cycles that were performed in parallel (updating the transition matrix, and some trial projections), and certain assumptions were made for other overhead costs. The overall approximate Full Modeled Cycles/All Cycles ratio was to 0.19% after  $\sim 0.677$  million cycles, and 6% after nearly 1.43 million cycles, which is nearing the end of the battery discharge. Calculations are based on use of a quad core computer for processing. This numerical cost is based heavily on the equipment and projection/error algorithm. For example, if more cores were available for processing the transition matrix could be updated more quickly, or if more error was allowed larger projections could be made, both

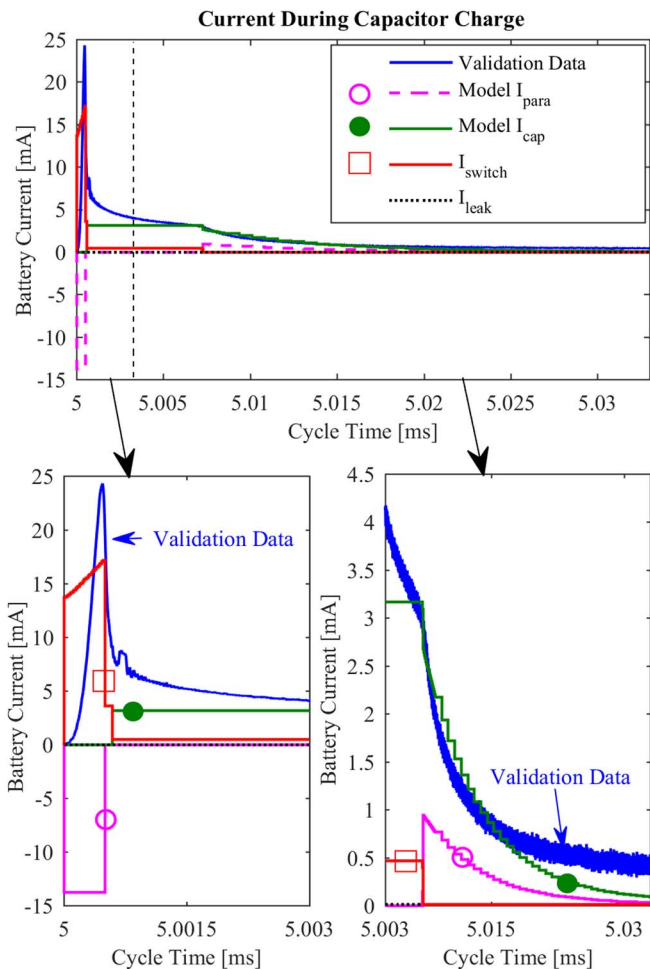


**Figure 13.** Current comparison. The initial part of capacitor charging is shown comparing the validation current<sup>19</sup> and the different components of the model current. Leakage current is small compared to other currents. The large current spike is due to the discharge of the parasitic capacitor. Circle and square symbols are to distinguish different profiles. (Lower) Detailed split view with different scales.

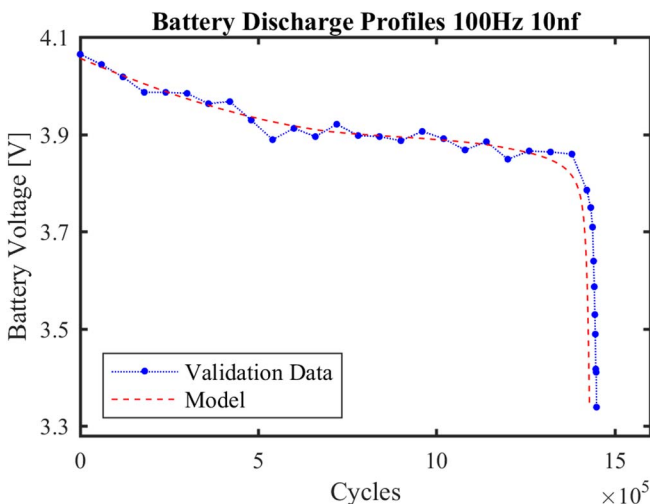


**Figure 14.** Discharge profiles. The discharge profiles of voltage just before capacitor charge are shown for the model and validation datasets.

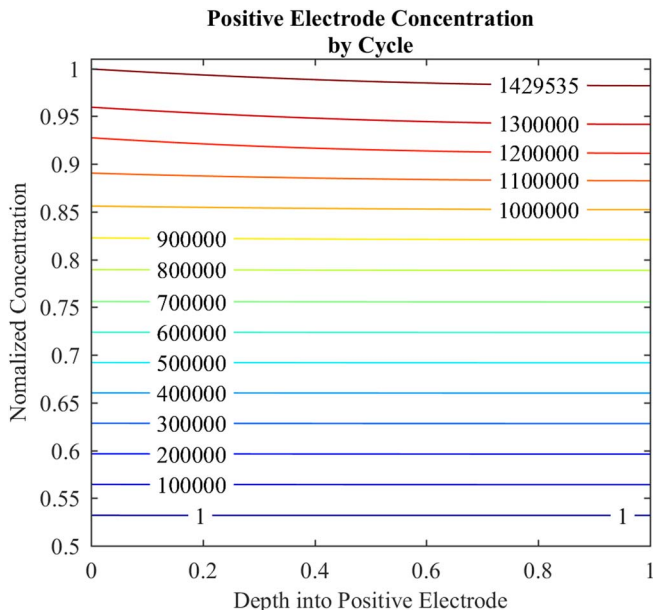


**Figure 15.** Positive electrode concentration profile by cycle. Normalized concentration profiles for the positive electrode over the full discharge of the battery. Labels indicate cycle number.

of which would reduce the numerical cost. Additionally, other approaches to numerical reduction are possible. For example, it may be possible to do a hybrid constant equivalent current projection (which would likely have greater success where the battery is able to recover between switching events like in this work); however, the proposed approach allows us to determine a benchmark for future work in full battery discharge modeling. Ultimately the projection is useful here to enable us to see the evolution of the modeled cycle profile over the battery discharge and validate the cyclic capacitive discharge model.

**Conclusions**

Cyclic capacitive loading of solid-state batteries in the mid-frequency range are of importance in areas such as MEMS. Here we review the fundamental electrochemical equations that define this type of system and the basic model presented by Fabre et al.<sup>2</sup> and Danilov et al.,<sup>20</sup> and the phenomena discussed in our previous work.<sup>19</sup> The underlying battery model was found to be suitable for capturing fast dynamics of individual charge cycles with some parameter adjustment, provided that all aspects of switching losses and parasitic loads were assessed/incorporated. We provide and demonstrated a hybrid parameter fitting framework where limited cyclic data can be used in connection with full discharges at constant current to capture fast and slow dynamics of the system. We developed and demonstrated a projection approach that can capture cyclic data from a limited number of cycles and project that over many cycles to significantly reduce the computational expense of fully modeling these systems. Finally, we implement these into a full battery cyclic model. We were able to show changes in cycle profiles over time with reasonable fitting of the battery discharge. Further work can be done to look at a broader set of loading conditions (capacitance and frequency, particularly higher average currents where the battery is not able to settle as much during cycling), as well as understanding the limitations of and improving the projection approach described here. Overall this work highlights the issues with cyclic capacitive loads, provides a modeling approach to describe these systems, and a projection approach allowing tracking of the cyclic profile over a battery discharge at reduced numerical cost.

### Acknowledgments

Research supported by National Science Foundation grants NSF CMMI 0954422 and NSF CMMI 1435222.

### List of Symbols

Symbol	Description	Units
A	Area	[m <sup>2</sup> ]
C	Capacitance	[F]
c	Concentration	[ $\frac{\text{mol}}{\text{m}^3}$ ]
D	Diffusion coefficient	[ $\frac{\text{m}^2}{\text{s}}$ ]
D <sub>0</sub>	Nominal diffusion coefficient	[ $\frac{\text{m}^2}{\text{s}}$ ]
F	Faraday's Constant	[ $\frac{\text{C}}{\text{mol}}$ ]
I	Current	[A]
I <sub>Leak</sub>	Leakage current through the switching circuitry	[A]
I <sub>Switch</sub>	Current lost through switching	[A]
i <sub>0</sub>	Exchange current density electrode/electrolyte interface	[ $\frac{\text{A}}{\text{m}^2}$ ]
L	Thickness	[m]
R	Universal gas constant	[ $\frac{\text{J}}{\text{mol}\cdot\text{K}}$ ]
R <sub>switch</sub>	Approximate resistance in limited path to ground during t <sub>charge</sub> -t <sub>comp</sub>	[Ω]
T	Temperature	[K]
T	Transition matrix	
t	Time	[s]
t <sub>charge</sub>	Time at beginning of capacitor charge	[s]
t <sub>comp</sub>	Time at switching completion	[s]
t <sub>hold</sub>	Time at beginning of the delay	[s]
t <sub>switch</sub>	Time at switch initiation	[s]
U	Open circuit potential	[V]
V	Voltage	[V]
V <sub>Batt</sub>	Battery Voltage	[V]
V <sub>Batt,Nom</sub>	Nominal battery voltage at full charge (4.1V)	[V]
V <sub>th</sub>	Switching threshold voltage	[V]
x	Spatial coordinate	[m]
y	Normalized li concentration	[-]

### Greek

α	Charge transfer coefficient	[-]
δ	Normalized concentration perturbation size for transition matrix construction	[-]
ε	Normalized concentration perturbation effect	[-]
κ	Conductivity	[S]
π	Non-dimensional parameter	[-]
φ	Coefficient for normalization	Varies

### Subscripts/Superscripts

+/-	Positive negative electrode
a	Anodic
c	Cathodic
cap	Load capacitor
e	Electrolyte

k	Total number of spatial grid points in finite difference
linear	Time during which the load capacitor has an approximate linear charge
m, i	Finite difference spatial grid point
max	Max value possible
n	Cycle number
p	Number of cycles projected
para	Parasitic capacitor

### References

1. M. Ghaed, G. Chen, R. Haque, M. Wieckowski, Y. Kim, G. Kim, Y. Lee, I. Lee, D. Fick, D. Kim, M. Seok, K. Wise, D. Blaauw, and D. Sylvester, *IEEE Trans. Circuits Syst. I*, **60**, 3152 (2013).
2. S. Fabre, D. Guy-Bouyssou, P. Bouillon, F. Le Cras, and C. Delacourt, *J. Electrochem. Soc.*, **159**, A104 (2012).
3. X. Hu, S. Li, and H. Peng, *J. Power Sources*, **198**, 359 (2012).
4. K. Takada, *Acta Mater.*, **61**, 759 (2013).
5. J. Oudenhoven, L. Baggetto, and P. Notten, *Adv. Energy Mat.*, **1**, 10 (2011).
6. Y. Zhou, M. Xue, and Z. Fu, *J. Power Sources*, **234**, 310 (2013).
7. A. Patil, V. Patil, D. Shin, J. Choi, D. Paik, and S. Yoon, *Mater. Res. Bull.*, **43**, 1913 (2008).
8. K. Cook-Chennault, N. Thambi, and A. Sastry, *Smart Mater. Struct.*, **17** (2008).
9. A. Vu, Y. Qian, and A. Stein, *Adv. Energy Mat.*, **2**, 1056 (2012).
10. K. Chen, Y. Shen, Y. Zhang, Y. Lin, and C. Nan, *J. Power Sources*, **249**, 306 (2014).
11. J. Kim, B. Son, S. Mukherjee, N. Schuppert, A. Bates, O. Kwon, M. Choi, H. Chung, and S. Park, *J. Power Sources*, **282**, 299 (2015).
12. Y. Wang, B. Liu, Q. Li, S. Cartmell, S. Ferrara, Z. Deng, and J. Xiao, *J. Power Sources*, **286**, 330 (2015).
13. T. F. Fuller, M. Doyle, and J. Newman, *J. Electrochem. Soc.*, **141**, 982 (1994).
14. L. M. Feeney, C. Rohner, P. Gunningberg, A. Lindgren, and L. Andersson, in *proceedings Wireless On-demand Network Systems and Services (WONS)*, 49 (2014).
15. S. Park, A. Savvides, and M. Srivastava, in *proceedings International Symposium on Lowpower Electronics and Design (IsLped)*, 382 (2001).
16. S. Castillo, N. Samala, K. Manwaring, B. Izadi, and D. Radhakrishnan, in *proceedings International Conference on Embedded Systems and Applications (ESA)*, 18 (2004).
17. K. Oldham, B. Edamana, and B. Hahn, in *proceedings ASME Dynamic Systems and Control Conference (DSCC)* (2011).
18. C. Rhee, J. Puskamp, R. Polcawich, and K. Oldham, *J. Microelectromech. Syst.*, **21**, 1492 (2012).
19. K. Teichert and K. Oldham, in *proceedings IEEE International Conference on Advanced Intelligent Mechatronics (AIM)*, 1610 (2016).
20. D. Danilov, R. Niessen, and P. Notten, *J. Electrochem. Soc.*, **158**, A215 (2011).
21. K. E. Thomas, J. Newman, and R. Darling, in *Advances in Lithium-ion Batteries*, W. van Schalkwijk and B. Scrosati Editors, ch. 12, pg. 362, Kluwer Academic Publishers, New York, 2002.
22. A. Rahmoun and H. Biechl, *Przegl. Elektrotech.*, **88**, 152 (2012).
23. M. Greenleaf, H. Li, and J. Zheng, *J. Power Sources*, **270**, 113 (2014).
24. H. He, R. Xiong, and J. Fan, *Energies*, **4**, 582 (2011).
25. S. K. Rahimian, S. Rayman, and R. E. White, *J. Power Sources*, **196**, 8450 (2011).
26. Cymbet Corporation, online <http://www.cymbet.com/pdfs/DS-72-41.pdf>.
27. M. Park, X. Zhang, M. Chung, G. Less, and A. M. Sastry, *J. Power Sources*, **195**, 7904 (2010).
28. K. Salloux, J. Lim, B. Dunn, P. Chaplya, and G. Carman, *J. Intell. Mater. Syst. Struct.*, **11**, 930 (2000).
29. B. Hahn, "Energy Efficient Iterative Adaptive On-Off Control of Capacitively-Loaded Actuators for Micro-robots," PhD, Mechanical Engineering, University of Michigan, (2012).
30. A. Deshpande, S. Phul, and B. Krishnamurthy, *J. electrochem. Sci. Eng.*, **5**(3), 181 (2015).
31. R. L. Spencer and M. Ware, *Ch. 8 Partial Differential Equations (in Computational Physics 430, Course Packet)*, Department of Physics and Astronomy, Brigham Young University, (2012).
32. M. Bowen and R. Smith, *Proc. R. Soc. A*, **461**, 1975 (2005).